ADVANCED FUNCTIONAL MATERIALS
www.afm-journal.de

Orientation Dependent Interlayer Coupling in Organic–Inorganic Heterostructures

*Cian Bartlam, Nihit Saigal, Stefan Heiserer, Hendrik Lambers, Ursula Wurstbauer, and Georg S. Duesberg**

Organic–inorganic 2D heterostructures combine the high optical absorption of organic molecules with exciton-dominated optical properties in layered transition metal dichalcogenides (TMDs) such as MoS_2. Critical to the interaction and the optical response in such hybrid systems is the electronic band alignment at the interface between the two species. Here, the coupling of monolayers of perylene derivatives is investigated with bilayer MoS_2. In particular, variation in the perylene orientation on the MoS_2 surface is identified using Raman spectroscopy and scanning probe microscopy. Low-temperature optical spectroscopy reveals orientation-dependent interlayer exciton formation. Furthermore, power-dependent photoluminescence measurements provide insight into the modified interlayer charge transfer in these heterostructures. A saturation of interlayer states is found under high excitation power when the perylene molecules are in a perpendicular orientation to the surface that leads to electron accumulation in the MoS_2, whereas parallel alignment of the perylene molecules leads to enhanced populations of organic–inorganic interlayer excitons. This work provides insights into the optimization of organic–inorganic heterostructures, with particular relevance to applications for optoelectronic and excitonic devices.

1. Introduction

Transition metal dichalcogenides (TMDs) have emerged as candidates for next-generation optical devices, hosting a range of novel optoelectronic properties even at room temperature.[1–3] A general feature of these systems is the hosting of excitonic states with high binding energies which, through type-II band alignment with other layers, can result in spatial separation of charge carriers by charge transfer (CT).[4] Artificially stacking TMD layers offers a way to modulate these properties, such as the control of interlayer (IL) excitons with characteristic low-energy features in their emission spectra.[5,6] Current challenges for TMD-TMD heterostructures include the strong dependencies of IL excitons on stacking alignment/twist angle[7] and variations in IL coupling in the presence of contamination[8] leading to extrinsically mediated recombination.[9]

Organic semiconductors, such as perylene derivatives, have been shown to noncovalently interact with group VI TMDs, resulting in organic–inorganic heterostructures that modulate the electronic and optical properties of the 2D material.[10–13] Properties of those systems include increased photocurrent generation due to higher charge carrier separation, doping via CT, and the quenching or enhancement of photoluminescence (PL) depending on the band alignment. This is in turn dependent on both the structure and conformation of the adsorbed molecular derivative.[14,10] This dependence allows a high level of tunability of the heterostructure. While hybridization and the formation of CT excitons between TMDs and organic molecules has been proposed,[15,16] upon photoexcitation competing CT mechanisms result in a combination of either free carrier generation upon Dexter-type CT or the formation of IL bound excitons.[17] Differences in band bending at the interface when comparing TMD monolayers to bulk crystals has been shown to generate free charge carriers in the monolayer case, whereas IL excitons form in the bulk,[18] allowing a combination of these phenomena to be studied in few-layer and bilayer TMDs coupled to organic molecules. Understanding the interaction at the interface of these organic–inorganic heterostructures is therefore crucial to the understanding of CT mechanisms in these systems.[19]

C. Bartlam, S. Heiserer, G. S. Duesberg
Institute of Physics
Faculty of Electrical Engineering and Information Technology & SENS Research Center
University of the Bundeswehr Munich
85579 Neubiberg, Germany
E-mail: duesberg@unibw.de

N. Saigal, H. Lambers, U. Wurstbauer
Institute of Physics
University of Münster
48149 Münster, Germany

U. Wurstbauer
Center for Soft Nanoscience (SoN)
University of Münster
48149 Münster, Germany

The ORCID identification number(s) for the author(s) of this article can be found under https://doi.org/10.1002/adfm.202315302

DOI: 10.1002/adfm.202315302

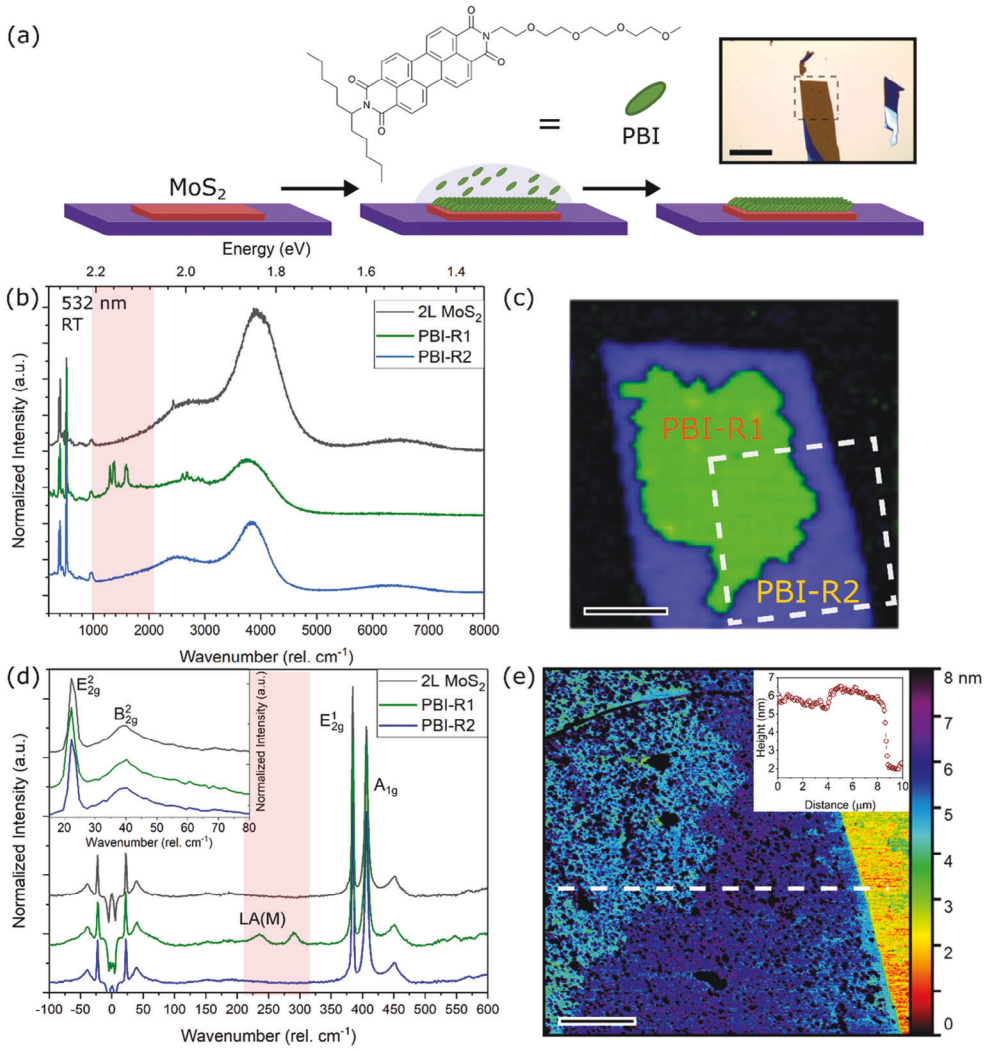

Figure 1. a) Functionalization scheme, structure of the PBI and optical micrograph of a functionalized bilayer MoS_2, 20 μm scale; b) RT PL spectra of unfunctionalized 2L MoS_2, and different regions of PBI functionalized 2L MoS_2, denoted as PBI-R1 and PBI-R2 normalized to the MoS_2 A_{1g} Raman mode at 532 nm excitation, red box highlights the frequency region of the PBI Raman modes; c) Intensity map of the highlighted components of the Raman spectra shown in b), showing destinct domains in green and blue corresponding to PBI-R1 and PBI-R2, repespectively. 5 μm scale; Dashed box shows the position of the AFM image shown in e), 5 μm scale; d) High resolution Raman spectra of 2L MoS_2, PBI-R1 and PBI-R2 at 532 nm excitation at RT, red box highlights the PBI and MoS_2 LA(M) Raman modes (521 cm^{-1} Si peak has been removed for clarity). Inset – low frequency and E^2_{2g} regions of the Raman spectra; e) AFM topographic image of the PBI-functionalized flake shown in c). The two domains of the PBI R1 and R2 in light and dark blue are visible,the borderline having the same shape as in the Raman in c). The dashed line shows the line profile shown in Inset, with a clearly visible step at the interface between the two domains, 2 μm scale. b,d) are vertically displaced for clarity.

Here we report on the optical properties of well-defined organic–inorganic heterostructures from perylene bisimide (PBI) derivatives on bilayer MoS_2 produced via deposition of the PBI molecules in liquid on mechanically exfoliated MoS_2. We identify the spectral features at both ambient and cryogenic temperatures that are due to variation in the molecular orientation of PBI on the surface of the 2D material. We show that PBI-bilayer MoS_2 systems with a high degree of orbital alignment can host IL excitons and that conversely poor orbital alignment results in reduced IL excitonic photoluminescence and decreased CT upon photoexcitation, highlighting the importance of molecular alignment of the organic layer at the interface.

2. Results and Discussion

2.1. Room Temperature Raman, Photoluminescence and AFM Analysis

In **Figure 1a**, the workflow for the assembly of the MoS_2-PBI heterostructures is depicted. In short, bilayer (2L) MoS_2 flakes were first micromechanically cleaved and transferred onto 70 nm thermally grown SiO_2/Si substrates. The layer number was determined using optical microscopy and the presence and position of the E^2_{2g} and B^2_{2g} Raman modes.[20] 2L MoS_2 was then functionalized by liquid phase deposition of PBI with a derivative which is soluble in organic solvents as detailed in the Experimental

Section. As a result the PBI selectively assembles onto TMDs as a monolayer as shown previously.[21]

PL and Raman measurements at room temperature (RT – 294 K, 532 nm) on a 2L MoS_2 flake before and after functionalization are shown in Figure 1b,d. The pristine MoS_2 spectrum, labelled 2L MoS_2, shows broad A and B exciton PL at 1.9 and 2.1 eV, respectively. After functionalization, the PL of the MoS_2 is significantly quenched across the heterostructure. However, the quenching is markedly different in distinct regions of the MoS_2 flake, denoted as PBI-R1 (green spectrum) and PBI-R2 (blue spectrum) with the spatial distribution of these areas highlighted in the Raman map shown in Figure 1c. For PBI-R2, both A and B exciton peaks show a reduction in intensity, while the A exciton spectral region shows higher quenching relative to the B exciton region in PBI-R1. Interestingly, the indirect PL intensity between 1.4–1.6 eV is similar for pristine 2L MoS_2 and PBI-R2 but is almost completely quenched in PBI-R1.

A strong perylene signature can be seen in the Raman spectrum in PBI-R1 region (Figure 1b). The modes at 1301, 1383, and 1587 cm^{-1} are assigned to the ring-breathing, Kekule and asymmetric modes of the polyaromatic perylene core[22] and emerge due to resonant exciton-phonon coupling and CT between the perylene molecules and the TMD.[14,23] The spectrum of PBI-R1 also shows additional modes at 235 and 290 cm^{-1}, highlighted in red in Figure 1d, which are assigned to the MoS_2 LA(M) mode and a PBI A_g mode originating from the perylene core,[24] respectively. The presence of the LA(M) mode indicates disorder-induced scattering[25] where perylene molecules are expected to hybridize with MoS_2 layers at this symmetry point.[16]

Atomic force microscopy (AFM) topographic imaging of the 2L MoS_2-PBI heterostructure, shown in Figure 1e, shows a clear contrast between the PBI-R1 and PBI-R2 regions identified in the Raman map of Figure 1c. Additional aggregates were found over the surface of the heterostructure due to crystallization from the PBI solution but could not be removed by further washing of the surface in THF. Signatures from these aggregates could not be detected in the optical measurements and mapping discussed above so can be seen to be decoupled from the MoS_2 surface in this regard. The step height from the underlying substrate to the heterostructure, averaging over 50 lines, is measured to be 3.0 ± 0.2 nm for PBI-R1 and 3.8 ± 0.2 nm for PBI-R2. This clearly indicates a different arrangement of the perylene derivatives in the respective regions. Ambient AFM of MoS_2 bilayers typically gives thicknesses ranging from 1.4–1.6 nm.[26] After subtraction, we then calculate an average PBI layer thickness in the range of 1.4–1.6 nm for PBI-R1 and 2.2–2.4 nm for PBI-R2, where PBI-R2 has a similar step height observed for self-aggregated perylene derivatives.[27]

After functionalization with PBI, the in-plane E^1_{2g} and out-of-plane A_{1g} Raman modes of MoS_2 (Figure 1d) were fitted with Lorentzian lineshapes and statistical analysis of the peak positions and full-width half maxima (FWHM) was performed over an area of the heterostructure. A downshift in the E^1_{2g} mode frequency can been observed in PBI-R1 by −0.3 ± 0.1 cm^{-1} (**Figure 2a**), showing higher MoS_2 lattice strain in this region.[28,29] This is further evidenced by an increase in the FWHM of the E^1_{2g} mode in PBI-R1 of 0.4 ± 0.2 cm^{-1} when compared to PBI-R2 (Figure 2b) as the degeneracy of this mode is lifted under strain.[28] The spatial distributions of the fitted E^1_{2g} peak parameters (Figure 2c,d) highlight that these changes are distinct between regions on the heterostructure. We do not observe any significant change in the A_{1g} frequency or width between regions, as expected for strain shifts in MoS_2 bilayers.[30]

Analysis of the IL MoS_2 Raman modes also shows clear spectral variation across the heterostructure. The FWHM of the E^2_{2g} in-plane shear mode at 22.8 cm^{-1} increases by 0.8 ± 0.4 cm^{-1} and is downshifted by −0.8 ± 0.1 cm^{-1} in PBI-R1, relative to PBI-R2 (Figure 2e–h). This splitting has been observed in MoS_2 bilayers due to a loss of symmetry under uniaxial strain.[30] E^2_{2g} shifts have been observed and calculated in Janus TMD structures due to changes in IL coupling due to increased dipolar interaction between the MoS_2 layers.[31] The out-of-plane B^2_{2g} IL mode centered at 41 cm^{-1} does not show any significant frequency shift between regions but shows a large increase in FWHM from ≈19 to 36 cm^{-1} (Figure 2i–l). It is expected that there is an additional contribution from the PBI molecule in this spectral region[24] giving rise to this significant broadening and limiting further analysis on peak position.

The reduction in the MoS_2 A exciton PL intensity at RT (Figure 1b), combined with the lack of a PBI Raman signature, demonstrates the presence of coupling between the PBI molecule and the MoS_2 orbitals in PBI-R2 but to a lesser degree than in the assembly in PBI-R1. This effect has been seen in coupled organic molecule-graphene heterostructures[32,33] where molecular symmetry was found to contribute to the Raman enhancement effect[34] which is sensitive to molecular orientation.[33] To further investigate this, low-temperature MoS_2 resonant Raman measurements at 632 nm excitation were performed (Figure S1, Supporting Information). The 290 cm^{-1} A_g perylene mode observed in Figure 1d has a reduced intensity in PBI-R1, as to be expected for this Raman enhancement mechanism, away from resonance with the perylene absorption.[23] PBI-R2 shows the presence of this mode under these conditions, indicating higher levels of intermolecular interaction (Figure S1, Supporting Information).[35] These observations demonstrate the presence of two distinct orientations of the PBI molecules on the MoS_2 surface in the PBI-R1 and PBI-R2 regions. The emergence of the LA(M) Raman mode in the PBI-R1 Raman spectrum (RT, 532 nm, Figure 1d) is due to greater PBI-MoS_2 orbital overlap in this region through parallel alignment of the PBI molecules to the TMD surface,[16] further evidencing higher intermolecular interaction. This accounts for the strain-induced changes observed in the in-plane E^1_{2g} and E^2_{2g} Raman modes (Figure 2), from the interaction strength between the PBI core and the MoS_2 lattice as has been reported for TMD-graphene heterostructures.[36]

The AFM height difference between the two regions is below that of a monolayer, i.e., not additive. These measurements further suggest that the perylene molecules in PBI-R2 are arranged perpendicular to the surface as has been observed previously for PBI derivatives on graphene.[37] Perylene molecules have been shown to have a range of conformations when assembled from solution[38,39] and similar perylene bisimides have been shown to organize either parallel[40] or perpendicular to 2D surfaces with tilt angles ranging from 12°–62°.[37,41,42] The cleanliness of the 2D interface prior to functionalization is often critical to molecular assembly, as highlighted elsewhere[19] and surface contamination has been shown to affect organic

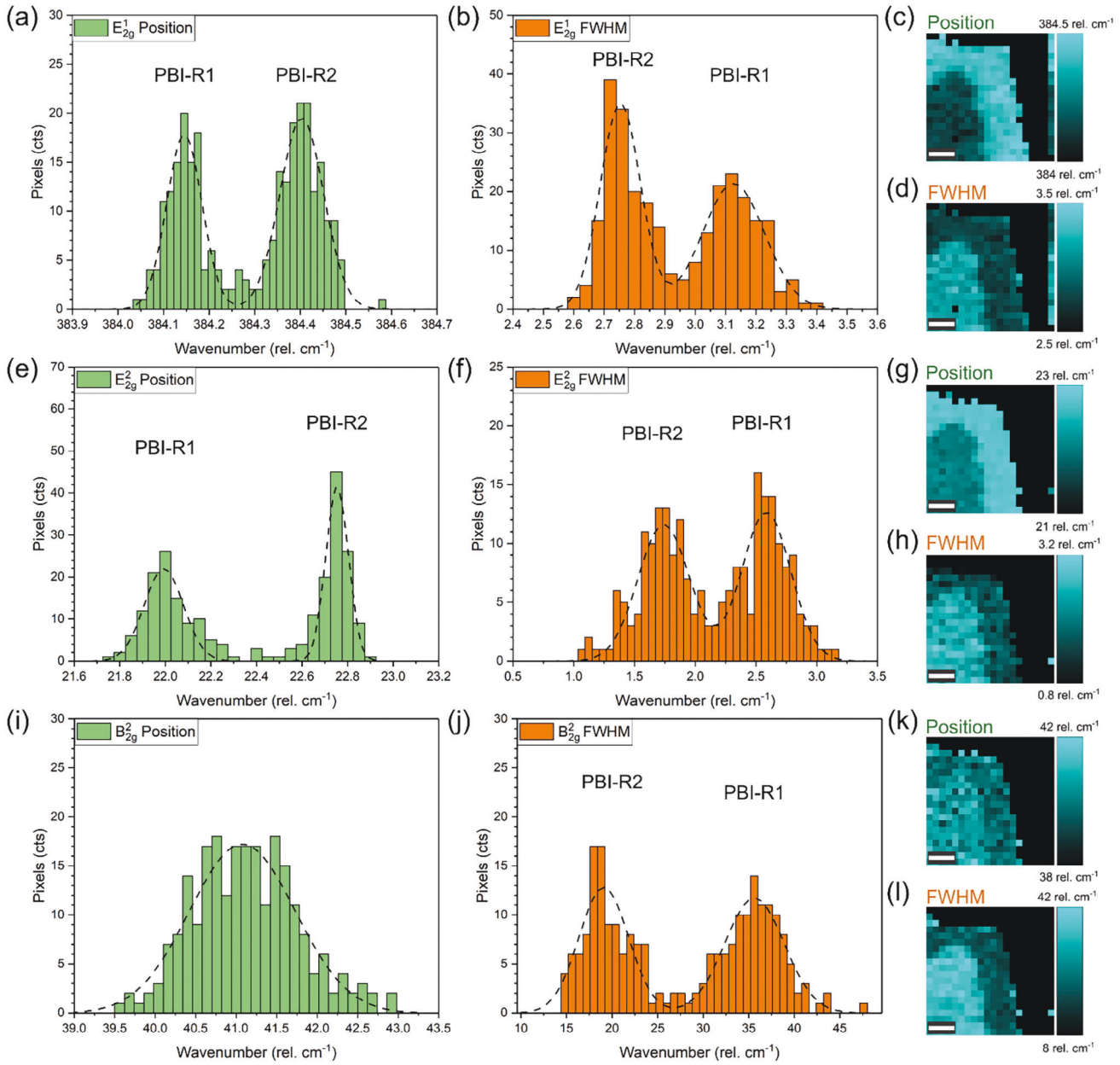

Figure 2. Statistical analysis of MoS_2 Raman modes of the PBI-MoS_2 heterostructure shown in Figure 1 (dashed lines, Gaussian fits): a) Histogram showing the frequency distribution of the E^1_{2g} mode; b) Histogram showing the FWHM distribution of the E^1_{2g} mode; c) Map of the E^1_{2g} frequency and d) FWHM; e) Histogram showing the frequency distribution of the E^2_{2g} mode; f) Histogram showing the FWHM distribution of the E^2_{2g} mode; g) Maps of the E^2_{2g} frequency and h) FWHM; i) Histogram showing the frequency distribution of the B^2_{2g} mode; j) Histogram showing the FWHM distribution of the B^2_{2g} mode; k) Map of the B^2_{2g} frequency and l) FWHM. Maps are shown with 2 µm scales.

packing on 2D materials resulting in changes in orientation.[43] The occurrence of the separate PBI-R1 and PBI-R2 phases is tentatively attributed to contamination on the MoS_2 surface prior to functionalization. MoS_2 crystals that were functionalized immediately after cleavage exclusively show the PBI-R1 conformation with planar arrangement of the PBI molecules (Figure S2, Supporting Information). Further investigation of the assembly mechanism may open a pathway for the controlled generation of different molecular arrangements on 2D surfaces.

2.2. Low Temperature Photoluminescence Spectroscopy

To further investigate the effect of the PBI orientation on the optical properties of the heterostructure, low temperature PL spectroscopy was performed. The 2L MoS_2 measured here exhibits a similar Raman and PL spectrum at RT to the unfunctionalized bilayer described above. **Figure** 3a shows low-temperature PL spectra (4 K) acquired at 1 µW excitation power under 532 nm illumination. The most striking differences between the spectra of 2L MoS_2 and PBI-R1, PBI-R2 is the quenching of the higher

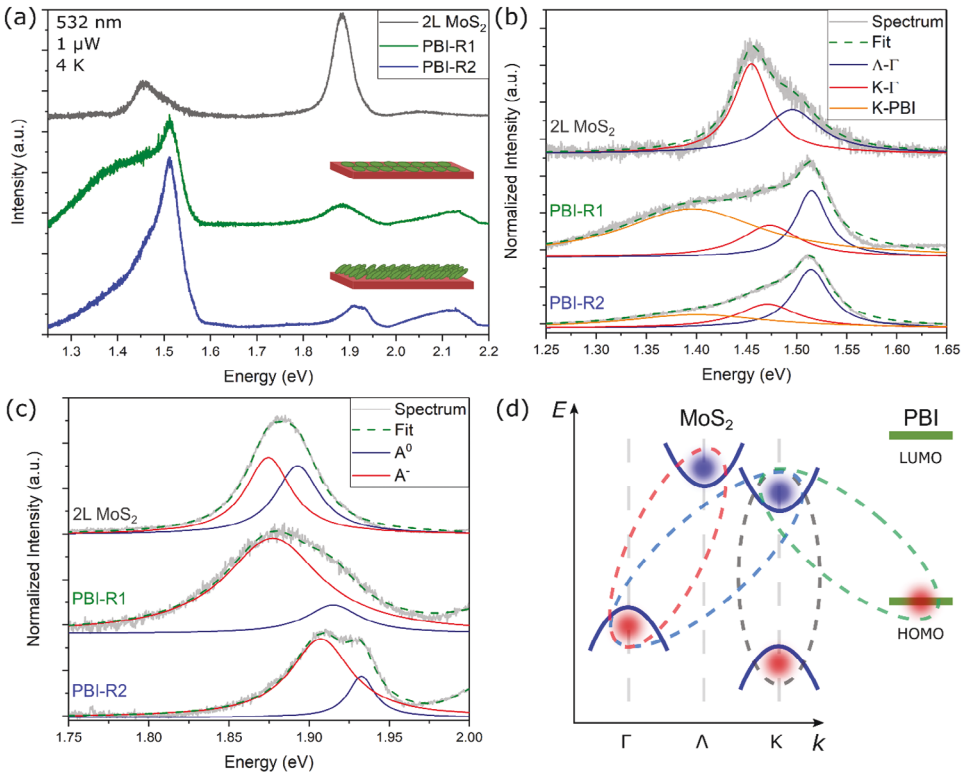

Figure 3. a) Steady state PL spectra of unfunctionalized 2L MoS_2, PBI-R1, and PBI-R2 (532 nm excitation wavelength, 1 μW power, temperature 4 K) with schematics of the different orientations of the PBI layer; b) Spectral fitting and components of the momentum indirect region (1.3–1.6 eV) of the PL spectra shown in a); c) Spectral fitting and components of the momentum direct region (1.8–1.95 eV) of the PL spectra shown in a); d) Schematic band diagram of PBI-functionalized bilayer MoS_2 showing the type-II alignment of the heterostructure and the location of electron–hole pairs. All plots are vertically displaced and the intensities of b,c) are normalized for clarity.

energy direct exciton emissions, a large increase in peak intensity between 1.3–1.6 eV, and the emergence of a low energy feature at 1.39–1.4 eV. The suppression of the direct emission after PBI functionalization is likely related to the CT between PBI and MoS_2 due to type-II band alignment at the heterostructure interface. Conversely, we attribute the large increase in the lower energy luminescence to suppression of nonradiative recombination which has been shown to occur as a result of functionalization.[44] Characteristic lower energy emissions are a typical feature of type-II band alignment in TMD-TMD heterostructures, where the staggered alignments of the conduction and valance bands results in an observed lower energy transition.[45] Analogous, hybrid CT states between organic molecules and TMDs have been predicted to occur upon functionalization,[16,46] where the molecular HOMO or LUMO takes on the role of a TMD band, providing energy minima across the two systems. The observed low-energy PL feature therefore provides a useful tool to probe the coupling between the PBI and MoS_2 layers with differing molecular orientation. For both PBI-R1 and PBI-R2, a large apparent increase PL intensity can be seen at 2.1 eV, seen more clearly at higher incident intensities (Figure S3a, Supporting Information) at the expected position of the MoS_2 B exciton. This feature originates from the 0→1 transition of the PBI molecule at 2.12 eV[23] which was confirmed by measuring free PBI on the surrounding substrate which gave the same peak shape and position (Figure S3a, Supporting Information).

Analysis of the 1.3–1.6 eV region of the unfunctionalized 2L MoS_2 PL spectrum, shown in Figure 3b, resolves features at 1.48 and 1.45 eV that originate from indirect intralayer recombination with electron–hole pairs residing at the Λ-Γ and K-Γ points, here referred to as $In_{\Lambda\text{-}\Gamma}$ and $In_{K\text{-}\Gamma}$ respectively.[47] In the case of PBI-R1 and PBI-R2, together with $In_{\Lambda\text{-}\Gamma}$ and $In_{K\text{-}\Gamma}$, a broad emission band below $In_{\Lambda\text{-}\Gamma}$ and $In_{K\text{-}\Gamma}$ is present. We assign this to a spatially indirect exciton at the interface of the MoS_2 and PBI adlayer, here labelled $IX_{K\text{-}PBI}$. The intensity of $IX_{K\text{-}PBI}$ differs sharply between PBI-R1 and PBI-R2, with PBI-R1 showing a much stronger contribution from $IX_{K\text{-}PBI}$ due to the increased orbital overlap in the parallel alignment as assigned previously.

The intralayer direct emission at ≈1.9 eV is composed of a charge-neutral A exciton, A^0, and a charged exciton (trion) contribution A^- (Figure 3c. The functionalized regions show a blueshift in A^0 of 28 and 38 meV for PBI-R1 and PBI-R2, respectively. Regarding PBI-R1, the A emission band (A^0 and A^-) is broad at low temperatures with the main contribution being from A^-. The FWHM of the A^- peak (80 meV) is approximately twice that in 2L MoS_2 (39 eV) and higher than in PBI-R2 (57 eV) indicating increased levels of interlayer CT.[48] For PBI-R2, the A^- (1.91 eV) emission peak can clearly be distinguished from the A^0 peak (1.93 eV) with the trion binding energy being calculated to be 26 meV under low excitation power (1 μW). The FWHM of A^0 in PBI-R2 shows a decrease of ≈20 meV upon functionalization. The reduction in FWHM for A^0 and A^- in the PBI-R2 region

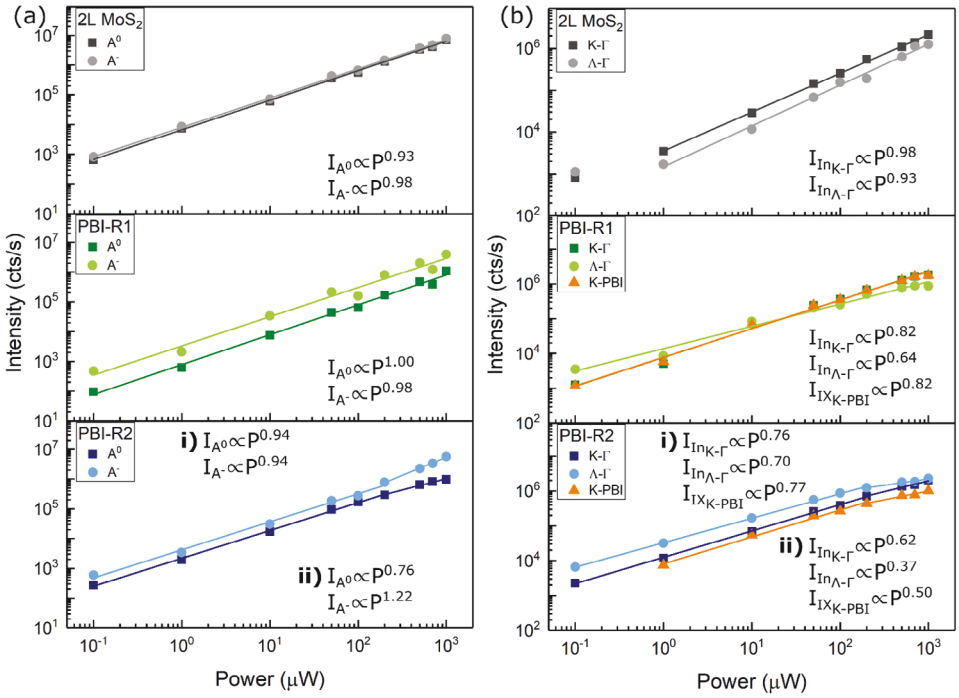

Figure 4. Power dependency of PL intensity for a) Momentum direct, and b) Momentum indirect transitions for 2L MoS_2, PBI-R1, and PBI-R2. Graphs include power law fits of intensity (I) as a function of power (P) and the calculated exponents of the respective data. i,ii) for PBI-R2 denote separate fits for low and high-power regimes.

together with the observed blueshift, when compared to 2L MoS_2 and PBI-R1, may originate from an increase in dielectric screening when PBI is in a perpendicular orientation and bandgap renormalization as a consequence.[49] All values for peak positions and widths are presented in Figure S3 and Table S1 (Supporting Information) with further discussion.

To identify the position of the photogenerated charge carriers within the heterostructure, measurements under non-resonant excitation conditions of the PBI were performed at 633 nm (Figure S3, Supporting Information). As this is below the excitation energy of PBI, any PL features observed originate predominantly from photoexcited electron–hole pairs within the MoS_2. We observe similar indirect spectral features to the measurements at 532 nm excitation for both PBI-R1 and PBI-R2, including the presence of $IX_{K\text{-}PBI}$ which, together with the relative increase in trion population compared to 2L MoS_2 (Figure 3c), would suggest that electrons accumulate in the MoS_2 bilayer and holes are concentrated in the PBI layer. Figure 3d shows a graphical schematic of the band alignment in the investigated 2L MoS_2-PBI heterostructures expected following literature calculations and the observations made in the analysis of the PL spectra. End group functionalization has been shown to have a minimal influence on the calculated HOMO and LUMO of PBI derivatives in most cases, giving ionization potentials (HOMO) of −5.9 to −6.0 eV and electron affinities (LUMO) of −3.6 to −3.5 eV for similar molecules, relative to the vacuum energy.[50] For 2L MoS_2, an ionization potential and electron affinity (i.e., valance band maximum (VBM) and conduction band minimum (CBM)) of −6.0 and −4.1 eV is expected respectively, based on GW calculations.[51] This would result in the type-II alignment observed here with a slight offset between the MoS_2 VBM at the Γ-point and PBI HOMO leading to the spectral features that can be observed here.

2.3. Photoluminescence Power Dependency

To gain further insight into the mechanisms of exciton generation and recombination between the two regions, the dependence of PL intensity (I) to laser excitation power (P) was measured and follows a power law relationship, $I \propto P^x$.[52] By analyzing the power dependency of the direct A and indirect emissions for 2L MoS_2 over a range of excitation powers (10^{-1}–10^3 μW) on a log-log scale (**Figure** 4a,b), all spectral features follow a near linear relationship with increasing power. The power law exponent close to 1 indicates monomolecular recombination for all direct transitions over broad range of incident power, as trion emission in this case is limited by hole population (Figure 4a). This is expected for MoS_2 deposited onto SiO_2 due to high levels of n-doping from the substrate that agrees well with the high intensity of the A^- trion emission shown in Figure 2d. Both momentum indirect transitions within 2L MoS_2 originating from a hole at the Γ point and an electron either at the K-point or Λ-point have almost identical power dependence, giving a near power independent transition probability for these indirect features (Figure 4b).

Regarding the functionalized regions, the fitted exponents of the momentum indirect recombination intensities for all transitions and structures are sublinear (Figure 4b) with $In_{\Lambda\text{-}\Gamma}$ being suppressed to the greatest degree upon functionalization, particularly at higher excitation powers. For PBI-R1, fitting of the direct

A° and A⁻ transitions indicates monomolecular recombination similar to 2L MoS_2, with an exponent close to 1 (Figure 4a). The IL exciton between an electron at the MoS_2 K valley and a hole at the PBI HOMO level is obviously only observable for the functionalized samples PBI-R1 and PBI-R2. In the low power regime (10^0–10^2 μW), the momentum indirect intralayer excitons show similar trends in the power dependent PL intensities as the IL excitons $IX_{K\text{-}PBI}$ for both types of heterostructure. At higher excitation powers, $IX_{K\text{-}PBI}$ shows a strong nonlinearity in PBI-R2 and a reduction in intensity when compared to $In_{K\text{-}\Gamma}$. We interpret this as a saturation of states due to the reduced orbital coupling between the PBI and MoS_2.

For PBI-R2, a similar linear relationship is seen for A^0 and A^- up to 100 μW (Figure 4a). The trion/exciton ratio, A^-/A^0, shows an increase in this region for both PBI-R1 and PBI-R2 compared to 2L MoS_2, from 1.2 to ≈4.2 and 1.8 for PBI-R1 and PBI-R2 respectively (Figure S4, Supporting Information). We assign this to a reduction in relative hole population in MoS_2 in PBI-R1 due to CT between the PBI and MoS_2, giving rise to a higher trion population.[53] This trend deviates in PBI-R2 under higher excitation intensities with a sharp increase of the A^-/A^0 ratio, at the same point as the reduction in indirect PL intensity discussed previously. This indicates a saturation in indirect recombination in the heterostructure where we propose the following mechanism:[54] Based on the observations discussed above, this inflection point signifies a limit on the IL hole transfer from MoS_2 to PBI due to the poor interfacial orbital overlap, effectively changing the donor-acceptor ratio due to a saturation of filled states.[52] The large increase in trion density within the MoS_2 would indicate that electron transfer from the PBI molecule continues, due to a continuum of accepting states at higher levels of the MoS_2 conduction band available for this process, whereas for hole transfer to PBI, the acceptor HOMO is localized and more sensitive to alignment. The increase in trion intensity is accompanied by a redshift in the peak energy of $IX_{K\text{-}PBI}$ (Figure S4, Supporting Information). Characteristically in TMD-TMD heterostructures, higher IL exciton populations result in a blueshift of the emission energy with increasing excitation power due to repulsive interactions between static out-of-plane IL excitonic dipoles.[55] As this is not observed for PBI-R1 in the power range investigated here, it is possible that this redshift comes from screening due to the increased electron population in the MoS_2 layer, however the exact mechanism warrants further investigation.

3. Conclusion

In this work, we report on the modulation of the optical emission properties of 2L MoS_2 upon noncovalent functionalization with a PBI monolayer, forming an organic–inorganic heterostructure. Domains with different orientations of PBI have been identified using in-depth Raman spectroscopic characterization. The regions extend over several micrometers and show distinctly different properties. Perylene orientation-dependent PL quenching at room temperature is observed, which we have attributed to different levels of CT efficiency in type-II alignment, and nonradiative recombination. We observe increased strain in the MoS_2 lattice in areas of high orbital alignment of the PBI molecules with the MoS_2 lattice. Notably, RT Raman mapping allows for rapid and simple evaluation of the molecular alignment and organic layer coupling. At low temperatures, PL measurements show the emergence and stabilization of IL excitons between the organic and inorganic layers. The intensity of these indirect emission signatures show dependence on the molecular orientation of the perylene film and orbital overlap with MoS_2 and excitation power. We find that under high excitation power, CT becomes saturated in the case when the PBI molecules have reduced orbital overlap with the surface, leading to increased trion densities. The study has implications for both fundamental understanding of the spectroscopy of these materials, the control of photogeneration of charge carriers in these systems, and for optoelectronic devices based on 2D organic–inorganic heterostructures.

4. Experimental Section

2D MoS_2 flakes were produced by mechanical cleavage of bulk crystals (HQ Graphene) onto 70 nm thermally grown SiO_2/Si substrates using Nitto tape. The substrate was sonicated in acetone, DI water and IPA followed by oxygen plasma treatment immediately before exfoliation to remove any surface contamination. The SiO_2 thickness was chosen in order to increase the optical contrast of the MoS_2 to aid the identification of thinned layers.[56] The MoS_2 flakes were first characterized at room temperature without any chemical treatment, and then selectively functionalized with N-(1-pentylhexyl)-N′-(3,6,9,12-tetraoxatridecyl)perylene-3,4:9,10-bisimide (PBI) using wet chemical deposition. Similar to methods described previously,[21] the sample was immersed into a 0.1 mM PBI solution in THF for 16 h. The functionalized material was then repeatedly washed in THF and IPA before drying under nitrogen. The freshly cleaved samples were functionalized in the same manner but were not subjected to characterization before PBI deposition, to limit the exposure of the MoS_2 surface to ambient adsorbates.

All RT optical measurements were carried out at 21 °C on a WITec Alpha300 R Raman microscope (Oxford Instruments) with a temperature-controlled stage (Linkham THMS 600). RT PL and Raman measurements were performed with a 532 nm laser line using either a 600 or 1800 gr mm^{-1} diffraction grating. Component analysis and extraction was carried out using multivariate analysis in WITec Project FIVE software. AFM imaging was performed using a Jupiter XR microscope (Asylum, Oxford Instruments) operating in AC mode with an AC-240TS-R3 cantilever. The AFM images were processed using Gwyddion 2.60 including subtraction of the contribution of aggregated material from the step height.

For low temperature measurements, the samples were cooled to 4 K in a Bluefors dilution refrigerator with optical access. The samples were excited using either 532 or 632 nm wavelength lasers. PL and Raman spectroscopy was performed using a home-built setup consisting of a triple grating spectrometer in a subtractive mode coupled to a liquid Nitrogen cooled CCD. In the case of PL measurements, the gratings used were 300, 300, and 600 gr mm^{-1} for the three spectrometer stages respectively. For the circular polarization resolved Raman measurements, 2400 gr mm^{-1} gratings were used for all the three spectrometer stages. Quarter waveplates of appropriate wavelength range were introduced in both the excitation and detection paths. All PL spectra were fitted with Lorentzian functions.

Supporting Information

Supporting Information is available from the Wiley Online Library or from the author.

Acknowledgements

C.B., S.H., and G.S.D. would like to acknowledge funding from the European Union's Horizon 2020 research and innovation program under grant

agreements No. 881603 (Graphene Flagship), No. 101046693 (SSLiP), and No. 10113596 (2D-PRINTABLE). Further, the authors thank dtec.bw—Digitalization and Technology Research Center of the Bundeswehr for support (project VITAL-SENSE). dtec.bw was funded via the German Recovery and Resilience Plan by the European Union (NextGenerationEU). U.W., N.S., and H. L. would like to acknowledge founding from the German Science Foundation (DFG) for financial support via Grant WU 637/4-2.

Open access funding enabled and organized by Projekt DEAL.

Conflict of Interest

The authors declare no conflict of interest.

Data Availability Statement

The data that support the findings of this study are available from the corresponding author upon reasonable request.

Keywords

charge transfer, heterostructures, interlayer excitons, MoS_2, perylene, photoluminescence, self-assembly, 2D materials

Received: December 1, 2023
Revised: February 13, 2024
Published online: March 10, 2024

[1] K. F. Mak, K. He, C. Lee, G. H. Lee, J. Hone, T. F. Heinz, J. Shan, *Nat. Mater.* **2013**, *12*, 207.
[2] N. Peimyoo, T. Deilmann, F. Withers, J. Escolar, D. Nutting, T. Taniguchi, K. Watanabe, A. Taghizadeh, M. F. Craciun, K. S. Thygesen, S. Russo, *Nat. Nanotechnol.* **2021**, *16*, 888.
[3] N. Leisgang, S. Shree, I. Paradisanos, L. Sponfeldner, C. Robert, D. Lagarde, A. Balocchi, K. Watanabe, T. Taniguchi, X. Marie, R. J. Warburton, I. C. Gerber, B. Urbaszek, *Nat. Nanotechnol.* **2020**, *15*, 901.
[4] T. Deilmann, M. Rohlfing, U. Wurstbauer, *J. Phys. Condens. Matter* **2020**, *32*, 333002.
[5] T. Deilmann, K. S. Thygesen, *Nano Lett.* **2018**, *18*, 2984.
[6] B. Miller, A. Steinhoff, B. Pano, J. Klein, F. Jahnke, A. Holleitner, U. Wurstbauer, *Nano Lett.* **2017**, *17*, 5229.
[7] L. Yuan, B. Zheng, J. Kunstmann, T. Brumme, A. B. Kuc, C. Ma, S. Deng, D. Blach, A. Pan, L. Huang, *Nat. Mater.* **2020**, *19*, 617.
[8] J. J. Schwartz, H.-J. Chuang, M. R. Rosenberger, S. V. Sivaram, K. M. McCreary, B. T. Jonker, A. Centrone, *ACS Appl. Mater. Interfaces* **2019**, *11*, 25578.
[9] H. Zhu, J. Wang, Z. Gong, Y. D. Kim, J. Hone, X. Y. Zhu, *Nano Lett.* **2017**, *17*, 3591.
[10] S. M. Obaidulla, M. R. Habib, Y. Khan, Y. Kong, T. Liang, M. Xu, *Adv. Mater. Interfaces* **2020**, *7*, 1901197.
[11] Y. J. Zheng, Y. L. Huang, Y. Chen, W. Zhao, G. Eda, C. D. Spataru, W. Zhang, Y. H. Chang, L. J. Li, D. Chi, S. Y. Quek, A. T. S. Wee, *ACS Nano* **2016**, *10*, 2476.
[12] T. Zhu, L. Yuan, Y. Zhao, M. Zhou, Y. Wan, J. Mei, L. Huang, *Sci. Adv.* **2018**, *4*, 1.
[13] H. Kim, W. Kim, M. O'Brien, N. McEvoy, C. Yim, M. Marcia, F. Hauke, A. Hirsch, G. T. Kim, G. S. Duesberg, *Nanoscale* **2018**, *10*, 17557.
[14] S. Park, N. Mutz, S. A. Kovalenko, T. Schultz, D. Shin, A. Aljarb, L. J. Li, V. Tung, P. Amsalem, E. J. W. List-Kratochvil, J. Stähler, X. Xu, S. Blumstengel, N. Koch, *Adv. Sci.* **2021**, *8*, 2100215.
[15] Y. L. Huang, Y. J. Zheng, Z. Song, D. Chi, A. T. S. Wee, S. Y. Quek, *Chem. Soc. Rev.* **2018**, *47*, 3241.
[16] J. Krumland, C. Cocchi, *Electron. Struct.* **2021**, *3*, 044003.
[17] T. R. Kafle, B. Kattel, P. Yao, P. Zereshki, H. Zhao, W. L. Chan, *J. Am. Chem. Soc.* **2019**, *141*, 11328.
[18] Y. Guo, L. Wu, J. Deng, L. Zhou, W. Jiang, S. Lu, D. Huo, J. Ji, Y. Bai, X. Lin, S. Zhang, H. Xu, W. Ji, C. Zhang, *Nano Res.* **2022**, *15*, 1276.
[19] S. H. Amsterdam, T. J. Marks, M. C. Hersam, *J. Phys. Chem. Lett.* **2021**, *12*, 4543.
[20] L. Liang, J. Zhang, B. G. Sumpter, Q. H. Tan, P. H. Tan, V. Meunier, *ACS Nano* **2017**, *11*, 11777.
[21] R. Tilmann, C. Weiß, C. P. Cullen, L. Peters, O. Hartwig, L. Höltgen, T. Stimpel-Lindner, K. C. Knirsch, N. McEvoy, A. Hirsch, G. S. Duesberg, *Adv. Electron. Mater.* **2021**, *7*, 2000564.
[22] N. Chiang, N. Jiang, L. R. Madison, E. A. Pozzi, M. R. Wasielewski, M. A. Ratner, M. C. Hersam, T. Seideman, G. C. Schatz, R. P. Van Duyne, *J. Am. Chem. Soc.* **2017**, *139*, 18664.
[23] C. Muccianti, S. L. Zachritz, A. Garlant, C. N. Eads, B. H. Badada, A. Alfrey, M. R. Koehler, D. G. Mandrus, R. Binder, B. J. LeRoy, O. L. A. Monti, J. R. Schaibley, *J. Phys. Chem. C* **2020**, *124*, 27637.
[24] D. Tenne, S. Park, T. Kampen, A. Das, R. Scholz, D. Zahn, *Phys. Rev. B – Condens. Matter Mater. Phys.* **2000**, *61*, 14564.
[25] G. L. Frey, R. Tenne, M. J. Matthews, M. S. Dresselhaus, G. Dresselhaus, *Phys. Rev. B* **1999**, *60*, 2883.
[26] T.-X. Huang, X. Cong, S.-S. Wu, K.-Q. Lin, X. Yao, Y.-H. He, J.-B. Wu, Y.-F. Bao, S.-C. Huang, X. Wang, P. H. Tan, B. Ren, *Nat. Commun.* **2019**, *10*, 5544.
[27] Z. Chen, V. Stepanenko, V. Dehm, P. Prins, L. D. A. Siebbeles, J. Seibt, P. Marquetand, V. Engel, F. Würthner, *Chem. – A Eur. J.* **2007**, *13*, 436.
[28] C. R. Zhu, G. Wang, B. L. Liu, X. Marie, X. F. Qiao, X. Zhang, X. X. Wu, H. Fan, P. H. Tan, T. Amand, B. Urbaszek, *Phys. Rev. B – Condens. Matter Mater. Phys.* **2013**, *88*, 121301.
[29] B. Miller, E. Parzinger, A. Vernickel, A. W. Holleitner, U. Wurstbauer, *Appl. Phys. Lett.* **2015**, *106*, 122103.
[30] J.-U. Lee, S. Woo, J. Park, H. C. Park, Y.-W. Son, H. Cheong, *Nat. Commun.* **2017**, *8*, 1370.
[31] K. Zhang, Y. Guo, Q. Ji, A.-Y. Lu, C. Su, H. Wang, A. A. Puretzky, D. B. Geohegan, X. Qian, S. Fang, E. Kaxiras, J. Kong, S. Huang, *J. Am. Chem. Soc.* **2020**, *142*, 17499.
[32] X. Ling, J. Zhang, *Small* **2010**, *6*, 2020.
[33] X. Ling, J. Wu, W. Xu, J. Zhang, *Small* **2012**, *8*, 1365.
[34] S. Huang, X. Ling, L. Liang, Y. Song, W. Fang, J. Zhang, J. Kong, V. Meunier, M. S. Dresselhaus, *Nano Lett.* **2015**, *15*, 2892.
[35] D. L. Akins, *Nanomater. Nanotechnol.* **2014**, *4*, 4.
[36] J. W. Jiang, H. S. Park, *Appl. Phys. Lett.* **2014**, *105*, 033108.
[37] N. C. Berner, S. Winters, C. Backes, C. Yim, K. C. Dümbgen, I. Kaminska, S. Mackowski, A. A. Cafolla, A. Hirsch, G. S. Duesberg, *Nanoscale* **2015**, *7*, 16337.
[38] Y. J. Kim, Y. J. Kim, Y. Lee, K. Park, C. W. Ahn, H. T. Jung, H. J. Jeon, *J. Phys. Chem. Lett.* **2020**, *11*, 3934.
[39] M. Ogasawara, X. Lin, H. Kurata, H. Ouchi, M. Yamauchi, T. Ohba, T. Kajitani, T. Fukushima, M. Numata, R. Nogami, B. Adhikari, S. Yagai, *Mater. Chem. Front.* **2018**, *2*, 171.
[40] Y. Kaneda, M. E. Stawasz, D. L. Sampson, B. A. Parkinson, *Langmuir* **2001**, *17*, 6185.
[41] N. Mrkyvkova, M. Hodas, J. Hagara, P. Nadazdy, Y. Halahovets, M. Bodik, K. Tokar, J. W. Chai, S. J. Wang, D. Z. Chi, A. Chumakov, O. Konovalov, A. Hinderhofer, M. Jergel, E. Majkova, P. Siffalovic, F. Schreiber, *Appl. Phys. Lett.* **2019**, *114*, 251906.
[42] Arramel, X. Yin, Q. Wang, Y. J. Zheng, Z. Song, M. H. Bin Hassan, D. Qi, J. Wu, A. Rusydi, A. T. S. Wee, *ACS Appl. Mater. Interfaces* **2017**, *9*, 5566.
[43] W. H. Lee, J. Park, S. H. Sim, S. Lim, K. S. Kim, B. H. Hong, K. Cho, *J. Am. Chem. Soc.* **2011**, *133*, 4447.

[44] M. Amani, D.-H. Lien, D. Kiriya, J. Xiao, A. Azcatl, J. Noh, S. R. Madhvapathy, R. Addou, S. KC, M. Dubey, K. Cho, R. M. Wallace, S.-C. Lee, H. He Jr., J. W. Ager, X. Zhang, E. Yablonovitch, A. Javey, *Science* **2015**, *350*, 1065.
[45] E. V. Calman, M. M. Fogler, L. V. Butov, S. Hu, A. Mishchenko, A. K. Geim, *Nat. Commun.* **2018**, *9*, 1895.
[46] K. Ulman, S. Y. Quek, *Nano Lett.* **2021**, *21*, 8888.
[47] W. Zhao, R. M. Ribeiro, M. Toh, A. Carvalho, C. Kloc, A. H. Castro Neto, G. Eda, *Nano Lett.* **2013**, *13*, 5627.
[48] A. F. Rigosi, H. M. Hill, Y. Li, A. Chernikov, T. F. Heinz, *Nano Lett.* **2015**, *15*, 5033.
[49] A. Faridi, D. Culcer, R. Asgari, *Phys. Rev. B* **2021**, *104*, 085432.
[50] M. Carmen Ruiz Delgado, E. G. Kim, D. A. Da Silva Filho, J. L. Bredas, *J. Am. Chem. Soc.* **2010**, *132*, 3375.
[51] H. G. Kim, H. J. Choi, *Phys. Rev. B* **2021**, *103*, 085404.
[52] T. Schmidt, G. Daniel, K. Lischka, *J. Cryst. Growth* **1992**, *117*, 748.
[53] M. Z. Bellus, F. Ceballos, H. Y. Chiu, H. Zhao, *ACS Nano* **2015**, *9*, 6459.
[54] K. Rijal, F. Rudayni, T. R. Kafle, W. L. Chan, *J. Phys. Chem. Lett.* **2020**, *11*, 7495.
[55] P. Nagler, G. Plechinger, M. V. Ballottin, A. Mitioglu, S. Meier, N. Paradiso, C. Strunk, A. Chernikov, P. C. M. Christianen, C. Schüller, T. Korn, *2D Mater.* **2017**, *4*, 025112.
[56] C. Hsu, R. Frisenda, R. Schmidt, A. Arora, S. M. Vasconcellos, R. Bratschitsch, H. S. J. Zant, A. Castellanos-Gomez, *Adv. Opt. Mater.* **2019**, *7*, 1900239.